

Negative electronic compressibility in charge islands in twisted bilayer graphene

Robin J. Dolleman ^{1,*}, Alexander Rothstein ^{1,2}, Ammon Fischer ³, Lennart Klebl ⁴, Lutz Waldecker ¹,
Kenji Watanabe ⁵, Takashi Taniguchi,⁶ Dante M. Kennes ^{3,7}, Florian Libisch,⁸
Bernd Beschoten ¹ and Christoph Stampfer ^{1,2,†}

¹JARA-FIT and 2nd Institute of Physics, RWTH Aachen University, 52074 Aachen, Germany, EU

²Peter Grünberg Institute (PGI-9), Forschungszentrum Jülich, 52425 Jülich, Germany, EU

³JARA-FIT and Institut für Theorie der Statistischen Physik, RWTH Aachen University, 52074 Aachen, Germany, EU

⁴I. Institute of Theoretical Physics, University of Hamburg, Notkestrasse 9, 22607 Hamburg, Germany, EU

⁵Research Center for Functional Materials, National Institute for Materials Science, 1-1 Namiki, Tsukuba 305-0044, Japan

⁶International Center for Materials Nanoarchitectonics, National Institute for Materials Science, 1-1 Namiki, Tsukuba 305-0044, Japan

⁷Max Planck Institute for the Structure and Dynamics of Matter, Center for Free Electron Laser Science, 22761 Hamburg, Germany, EU

⁸Institute for Theoretical Physics, Vienna University of Technology, 1040 Vienna, Austria, EU



(Received 16 December 2022; revised 26 February 2024; accepted 25 March 2024; published 23 April 2024)

We report on the observation of negative electronic compressibility in twisted bilayer graphene for Fermi energies close to insulating states. To observe this negative compressibility, we take advantage of naturally occurring twist-angle domains that emerge during the fabrication of the samples, leading to the formation of charge islands. We accurately measure their capacitance using Coulomb oscillations, from which we infer the compressibility of the electron gas. Notably, we not only observe the negative electronic compressibility near correlated insulating states at integer filling, but also prominently near the band insulating state at full filling, located at the edges of both the flat and remote bands. Furthermore, the individual twist-angle domains yield a well-defined carrier density, enabling us to quantify the strength of electronic interactions and verify the theoretical prediction that the inverse negative capacitance contribution is proportional to the average distance between the charge carriers. A detailed analysis of our findings suggests that Wigner crystallization is the most likely explanation for the observed negative electronic compressibility.

DOI: [10.1103/PhysRevB.109.155430](https://doi.org/10.1103/PhysRevB.109.155430)

I. INTRODUCTION

Twisting two layers of graphene creates a moiré supercell with enlarged periodicity [1–4], leading to band insulating states at full filling ($\nu = \pm 4$, where ν represents the filling factor denoting the number of charge carriers per supercell) [5] and flattening of the electronic bands [2,4]. Near the so-called magic angle of $\approx 1.1^\circ$, the ratio of Coulomb repulsion to kinetic energy becomes maximized [6], giving rise to correlated insulating states at fractional fillings and integer values of ν [7–10]. When the carrier density is slightly tuned away from these integer filling factors, strongly interacting itinerant charge carriers emerge. The interaction strength of charge carriers is characterized by a dimensionless parameter known as the Wigner-Seitz radius r_s [11,12], given by

$$r_s = \frac{1}{\sqrt{\pi}} \frac{a}{a_B} = \frac{am^*e^2}{4\pi^{3/2}\epsilon_0\epsilon_r\hbar^2}. \quad (1)$$

Here, $a = 1/\sqrt{n}$ is the average distance between charge carriers, n the charge-carrier density, a_B the (effective) Bohr radius, ϵ_0 the vacuum permittivity, ϵ_r the effective relative dielectric constant of the material, \hbar the reduced Planck constant, m^* the charge-carrier effective mass, and e the elementary

charge. Near an energy gap, the low carrier density (and large a) together with a large m^* of itinerant charge carriers results in a large value of r_s . This high r_s is likely crucial for the formation of strongly correlated electronic phases in twisted bilayer graphene (tBLG), such as the superconducting phases adjacent to the correlated insulating states, the origin of which remains not fully understood [8,13–18]. However, precise measurements near these gaps pose challenges due to variations in the twist angle across the sample, which have been identified as a significant source of disorder in tBLG [6,9,14,19–21]. These variations give rise to twist-angle domains within the sample, characterized by relatively uniform twist angles but abrupt transitions at the boundaries [22,23]. Since the twist angle dictates the position of moiré-induced energy gaps, their locations vary within the sample, complicating efforts to maintain a uniform itinerant charge-carrier density and r_s across the sample geometry.

In this study we capitalize on the twist-angle variations to isolate single twist-angle domains, accurately quantify their charging energy, and extract the interaction strength between itinerant charge carriers. To achieve this we utilize tBLG heterostructures with varying sizes and geometries, as described in Sec. II. We demonstrate that the inherent twist-angle variations induce electrostatic confinement near the insulating states of tBLG (Sec. III). These confined regions function as charge islands, and we precisely measure their capacitance using Coulomb oscillations. An in-depth analysis of this

*dolleman@physik.rwth-aachen.de

†stampfer@physik.rwth-aachen.de

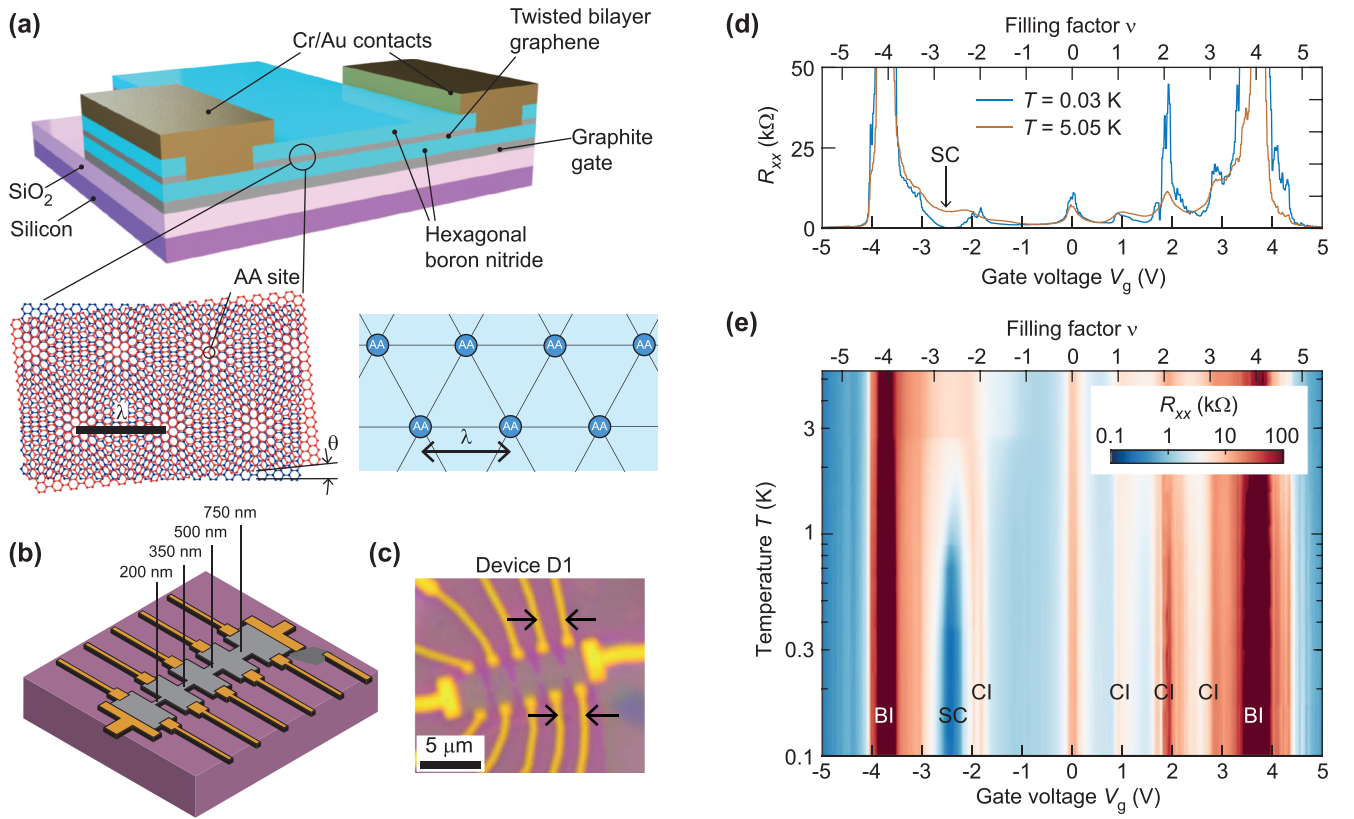


FIG. 1. (a) Schematic cross section of a tBLG device, including an illustration of the moiré lattice forming between the two graphene layers (bottom left) and the resulting stacking order (bottom right). Here, θ denotes the twist angle between the layers and λ the moiré wavelength. (b) Illustration of the constricted Hall-bar device D1, with the width of the constrictions labeled. (c) Optical microscopy image of device D1. (d) Four-point resistance as a function of gate voltage V_g and bulk filling factor ν at two temperatures (T), highlighting the fragile superconducting region (SC). (e) Four-point resistance as a function of gate voltage V_g and temperature of the 750-nm-wide constriction, measured with the contacts highlighted by arrows in panel (c). Band insulators (BIs), correlated insulators (CIs), and a fragile superconducting dome (SC) are visible.

capacitance reveals a negative electronic compressibility near both the band insulating states in the remote and flat bands, as well as near the correlated insulating states (Sec. IV). By fitting a model to the data, we find that the negative capacitance contribution is proportional to the square root of the charge-carrier density, consistent with expectations for correlated carriers. Furthermore, as the compressibility of the charge island remains unaffected by magnetic fields and is consistent among different bands, we propose that the observed negative compressibility is best explained by the formation of a Wigner crystal (Sec. V). Thus our technique provides insights into the intriguing properties of itinerant charge carriers in tBLG when the Fermi energy approaches the moiré-induced energy gaps.

II. SAMPLES AND SETUP

This study includes a total of six tBLG devices with different twist angles and geometries. The tBLG is created using either the “tear-and-stack” [5] or the “cut-and-stack” technique [24], generating a moiré pattern with periodicity λ , as illustrated in Fig. 1(a). The tBLG is encapsulated in hexagonal boron nitride (hBN), which serves as an atomically flat protective layer with electrical insulation [25]. To maintain a uniform electric field and minimize electrostatic potential

disorder, we utilize a graphite gate, promoting atomically flat interfaces [26,27]. For low-resistance one-dimensional contacts, we employ selective reactive-ion-etching and metallization techniques [28–30]. The resulting device structure is depicted in Fig. 1(a), and an example device is shown in Figs. 1(b) and 1(c). Further details on the fabrication process and devices are available in Appendix D.

In the main part of this work, we mainly show exemplary results from a specific device labeled D1, which incorporates a Hall-bar structure with constrictions, as shown in Figs. 1(b) and 1(c). These constrictions allow us to differentiate between edge and bulk confinement (see Supplemental Material S2 [31]). Within this device, we have implemented constrictions of varying widths: 750 nm, 500 nm, 350 nm, and 200 nm, denoted as C1, C2, C3, and C4, respectively.

To confirm the nature of the 750-nm-wide constriction C1 (Device D1) as tBLG, we analyze the temperature dependence of the resistance shown in Figs. 1(d) and 1(e). In this measurement, we can distinctly identify the band insulators (BI) positioned around the filling factor $\nu = \pm 4$. By pinpointing their precise locations in gate voltage and utilizing the gate lever arm, we can approximate the twist angle as $\theta \approx 1.02^\circ$ (see Appendix D). Moreover, in the vicinity of integer fillings of the partially occupied flat bands, we

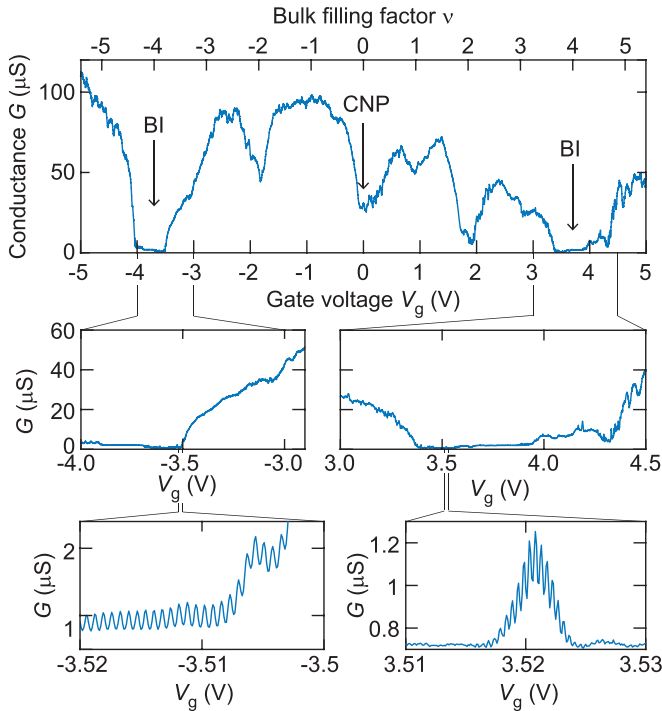


FIG. 2. Two-point conductance G as a function of gate voltage V_g over the entire gate voltage range. Zoom-ins close to the band insulating states reveal high-frequency conductance oscillations.

observe resistance peaks corresponding to fractional fillings $\nu = -2, 1, 2, 3$. These resistive features align with expectations for correlated insulating (CI) states [8,32]. Close to $\nu = -2.7$, the resistance exhibits a significant reduction with decreasing temperature, although it remains finite. This behavior indicates the presence of a fragile superconducting state [33] in the sample, as evidenced in the Supplemental Material S1 [31]. Furthermore, magnetotransport measurements (Supplemental Material S1 [31]) uncover the existence of Chern insulators featuring identical topological invariants to those reported in other studies of tBLG near the magic angle [24,34–38]. Consequently, we can conclude that our tBLG sample distinctly exhibits correlated phases akin to those observed in prior investigations near the magic angle [8,15–18,32].

III. CHARGE ISLANDS REVEALED BY COULOMB OSCILLATIONS

Each experiment which now follows consists of two-point conductance measurements where we increment the gate voltage in small steps to reveal high-frequency conductance oscillations. In Fig. 2 we show a conductance (G) trace obtained with 0.1-mV gate voltage steps measured across constriction C1. The charge neutrality point (CNP) at a filling factor of $\nu = 0$, and band insulators (BI) near full filling at $\nu = \pm 4$ are prominently visible within the trace. A zoom-in of the traces reveals regular high-frequency conductance oscillations at the transition towards the insulating states of our tBLG samples. These oscillations are observed in all our tBLG samples that show moiré-induced energy gaps (see Supplemental Material S2, S4, S5, S7 [31]).

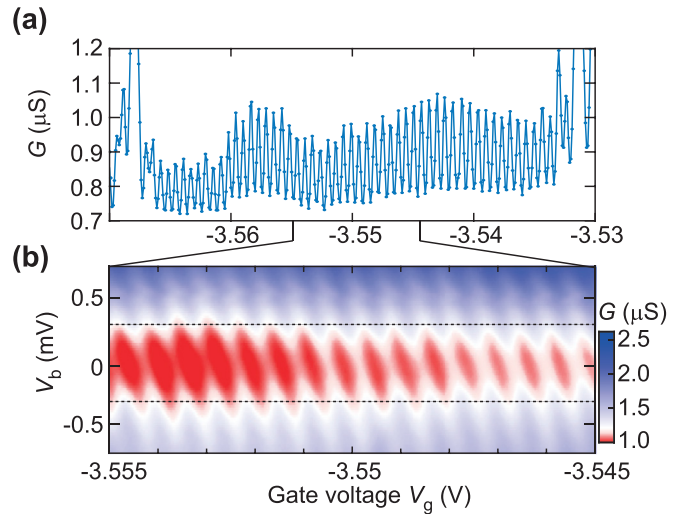


FIG. 3. (a) Exemplary two-point conductance (G) trace close to the band insulators or constriction C1. (b) Conductance as a function of gate voltage and bias voltage V_b in a small gate voltage range.

A. Dependence on bias voltage

To identify the origin of the conductance oscillations, we perform gate-dependent bias spectroscopy measurements, as illustrated in Fig. 3. The combined influence of bias and gate voltage forms a diamond-shaped region where the conductance is suppressed [Fig. 3(b)], a clear manifestation of the Coulomb blockade effect [39]. In the Coulomb blockade regime, transport is impeded by electrostatic repulsion within a region that confines charge carriers. If the bias potential eV_b is larger than the charging energy $E_c = e^2/C_\Sigma$, where C_Σ is the total capacitance of the charge island, the Coulomb blockade is lifted [40]. Due to the similarity in magnitude between the AC lock-in excitation (100 μ V root mean square) and the step size in bias and gate voltage, the sharp features of the Coulomb diamonds appear blurred. Nevertheless, we can extract the bias voltage (V_b) required to lift the blockade, which is $eV_b \approx \pm 0.31$ meV, as indicated by the dashed lines in Fig. 3(b).

The spacing between two Coulomb resonances on the gate-voltage axis is determined by two energy scales: the electrostatic charging energy and the quantum level spacing. The remarkable regularity of the measured Coulomb oscillations (Fig. 2) suggests that the charging energy dominates over the quantum level spacing. Therefore, the distance ΔV_g between the Coulomb resonances is given by $\Delta V_g = e/C$, where C represents the capacitance between the charge island and the graphite back gate [40,41]. From Fig. 3 we extract a periodicity of the oscillations $e\Delta V_g \approx 0.61$ meV. From this analysis we can conclude that $C \approx C_\Sigma/2$, suggesting that half of the total capacitance of the charge island arises from coupling to charge carriers in the source/drain leads.

B. Magnetic field dependence of the oscillations

Next we explore the behavior of the Coulomb oscillations under a perpendicular magnetic field B . We conduct measurements by sweeping the gate voltage in a narrow window while incrementally increasing the magnetic field. We observe a significant shift in Coulomb resonance positions [Fig. 4(a)],

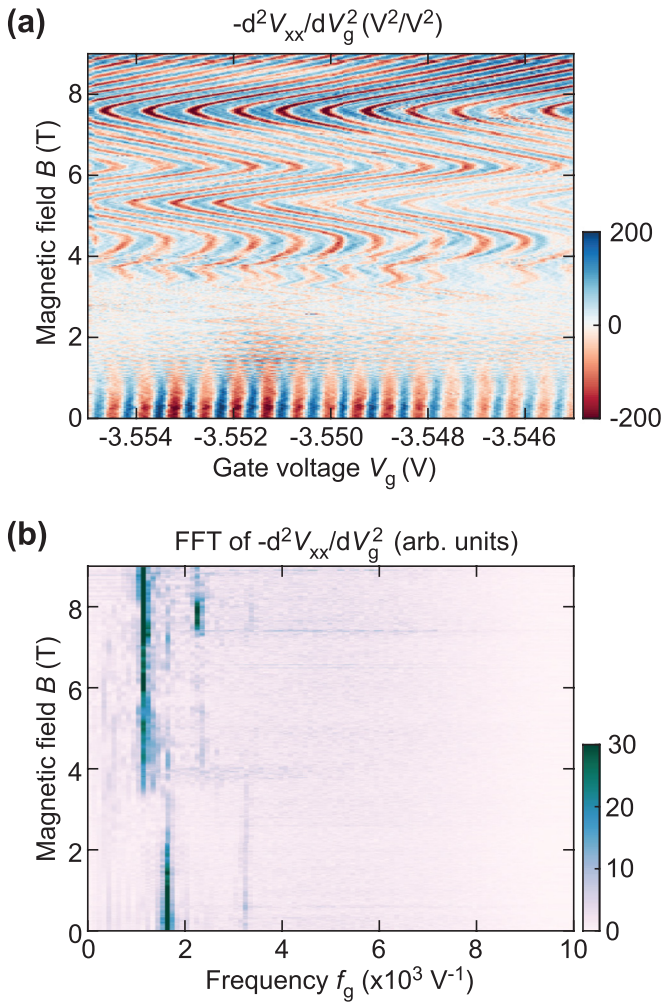


FIG. 4. Magnetic field dependence of the oscillations. (a) Gradient of the voltage drop (measured in the four-point configuration) as a function of gate voltage and magnetic field. (b) Power spectral density of the oscillations in panel (a) as a function of magnetic field.

while the spacing between them appears unaffected by the magnetic field. A fast Fourier transform (FFT) at each magnetic field reveals two distinct primary frequency components, with higher harmonics arising from the nonsinusoidal shape of the Coulomb resonance [Fig. 4(b)]. The power spectra's evolution with magnetic field displays a pronounced change in peak amplitude: the frequency component near 1600 V^{-1} decreases, and the component near 1100 V^{-1} becomes more prominent. As neither component fully disappears (which is evidenced by the phase coherence of both frequency components in the full magnetic field range, see Appendix A), they must originate from two distinct confined regions within the sample. The constant spacing further confirms that the charging energy dominates over the quantum level spacing in the Coulomb blockade effect. If the quantum level spacing were more significant, the single-particle energies would evolve differently due to the lifting of spin- and valley degeneracy with the magnetic field [42,43].

The position of the oscillations in Fig. 4(a) exhibits periodicity in $1/B$. This behavior, recently demonstrated in bilayer graphene quantum dots [44], can be explained by a classi-

cal electrostatic shift induced by density-of-states oscillations near the confined region. When the Fermi energy matches a Landau level, the density of states in the surrounding area increases, exerting a classical electrostatic force that shifts the energy levels inside the confined regions. Since an extremum in Fig. 4(a) signifies a constant electron density *inside* the confined region, the change in charge density must occur *outside* the confined region. Therefore these measurements provide valuable information about the Fermi surface of the carriers in the source/drain leads that couple to the charge island [44], further discussed in Appendix A.

C. Origin of the Coulomb oscillations

The presence of Coulomb oscillations requires an energy gap for charge confinement, such as a band gap, and spatial variations in the position of this gap relative to the Fermi level to create a confining potential for charge carriers. In Supplemental Material S2 [31], we investigate the Coulomb oscillations as a function of constriction width on device D1, finding a clear trend of Coulomb oscillations vanishing with decreasing sample width. This suggests that their origin lies in bulk characteristics rather than edge effects. Furthermore, the encapsulation of tBLG with hBN and the use of graphite gating should strongly suppress the effects of charge impurities and other potential disorder [27]. Therefore we propose that the confinements arise due to variations in the twist angle across the sample geometry [6,9,14,19–21], leading to the formation of twist-angle domains over the sample [22,23], as illustrated in Fig. 5(a). Local variations in the twist angle result in local changes in the energy gap offset relative to the Fermi level (see the potential landscape on the right-hand side of Fig. 5). Therefore, as the Fermi level approaches the band gap, certain domains become insulating earlier than others [Fig. 5(b)]. Close to the insulating state, individual domains may remain conducting while the surrounding area has already become insulating [Fig. 5(c)]. This scenario leads to individual charge islands and the observation of conductance oscillations as a function of gate voltage.

However, this leaves the question of how these charge islands are accessible in the transport experiment. An in-depth analysis of the quantum oscillation frequency in Appendix A reveals that the carriers tunneling in and out of the confinement exhibit a complete absence of moiré-induced energy gaps. This observation points toward an important role of the boundaries between twist-angle domains. Within these boundaries, strong disorder may be present on the length scale of the moiré superlattice. Consequently, locally, the moiré-induced gap may vanish, leaving charge carriers which tunnel in and out of the confinement. Since these boundaries are expected to appear over the entire sample geometry, we propose that they form a network that allows one to probe the local charge confinement in electronic transport experiments.

IV. NEGATIVE ELECTRONIC COMPRESSIBILITY

Next, we study the spacing of the Coulomb oscillations ΔV_g to determine the capacitance of the charge islands. Since $\Delta V_g = e/C$, the oscillation frequency f_g can be expressed as $f_g = C/e$, directly proportional to the back-gate capacitance

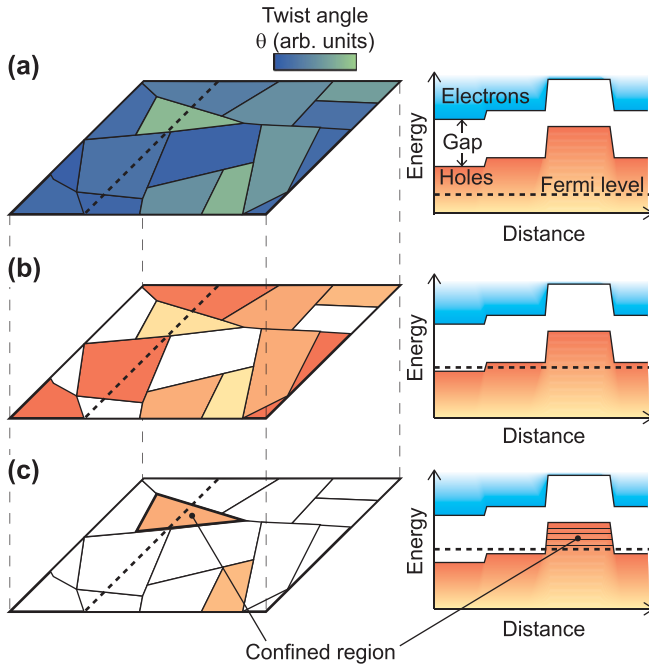


FIG. 5. Schematic illustration of twist-angle variations and resulting band structure variations over the sample geometry. (a) Illustration of the formation of twist-angle domains over the sample geometry, where the local variation of the band structure is drawn on the right-hand side. (b) The Fermi level increases, and in this example the areas with a small twist angle will become insulating since the Fermi level is in their band gap, while other areas remain conducting. (c) Further increasing the Fermi level results in the formation of confinements, where the energy levels are quantized.

of the charge island. To facilitate the analysis, we convert conductance traces to the frequency domain by calculating power spectra $P_\omega = |\mathcal{F}\{dG/dV_g\}|^2$, where \mathcal{F} represents the Fourier transform (for more details, see Appendix D). The resulting gate-voltage-dependent power spectra, presented in Fig. 6(a) for device C1, reveal multiple distinct frequency components near the insulating states (labeled as C1.1–C1.4), each corresponding to a single charge island. While the oscillation period remains regular within small gate voltage ranges (<10 mV), a continuous frequency tuning is evident on larger voltage scales. Across all tBLG devices in this study, we consistently observe an increase in frequency (and capacitance) as the Fermi level approaches the moiré-induced energy gap, representing a central result of our work (additional examples are presented in Supplemental Material S2, S4, S5, S7 [31]).

To elucidate the observed change in capacitance, we first consider the geometric capacitance C_g of the charge island within a parallel-plate capacitor model, given by $C_g = \epsilon_0 \epsilon_r A/d$, where A is the area of the island, and d is the distance between the tBLG and the graphite gate. Based on the twist-angle domain model outlined in Sec. III C and Fig. 5, we anticipate that A and C_g should remain constant as a function of gate voltage if the charge island consists of a single domain. However, if the charge island comprises multiple domains, we expect to observe a stepwise reduction of A and the capacitance. Alternatively, if the confinement arises from other types of potential disorder [45], we anticipate a

continuous reduction of the area A , as more of the surrounding area should become insulating when the Fermi level enters the band gap in the surrounding bulk. Given that these scenarios are inconsistent with our observations, we can conclude that the observed increase in capacitance is indicative of a negative compressibility of the charge carriers.

A. Models for the negative capacitance contribution

To investigate the negative compressibility contributing to the observed increase in capacitance, we consider two scenarios where negative compressibility can arise. First, we consider the exchange interaction in an electron gas, where the reduced likelihood of finding charge carriers with the same spin at the same position creates an “exchange hole” due to the opposite background charge [12,46,47]. The resulting negative interaction energy $E_{i,x}$ is given by

$$E_{i,x} = -\frac{e^2 A n^{3/2}}{3\sqrt{2}\pi^{3/2}\epsilon_0\epsilon'_r} [(1 + \xi)^{3/2} + (1 - \xi)^{3/2}], \quad (2)$$

where ξ represents the polarization of magnetic moments, ranging from 0 (unpolarized) to 1 (fully polarized). Secondly, we consider the case of a Wigner crystal, where charge carriers minimize their potential energy by forming a solid phase with a triangular lattice [48]. The resulting negative interaction energy $E_{i,w}$ is given by [48–53]

$$E_{i,w} = -\frac{\eta_T e^2 A n^{3/2}}{8\pi\epsilon_0\epsilon'_r}, \quad (3)$$

where $\eta_T = 3.92$ is a numerical constant associated with the triangular lattice.

In both scenarios the negative interaction energy E_i leads to a negative (thermodynamic) electronic compressibility κ , expressed as $\kappa^{-1} = d\mu/dn = (1/A)(d^2E_i/dn^2)$, where μ is the electrochemical potential. The negative compressibility contributes to a negative capacitance contribution C_i , where $C_i^{-1} = \kappa^{-1}/(Ae^2)$, increasing the total capacitance C beyond the geometric contribution C_g according to the relation [52,54–56]

$$C^{-1} = C_g^{-1} + C_i^{-1} = C_g^{-1} + \frac{1}{A^2 e^2} \frac{d^2 E_i}{dn^2}. \quad (4)$$

Since the carrier density dependence of both interaction energies is the same [Eqs. (2) and (3)], we can use Eq. (4) to obtain a general model for the capacitance, including the effect of correlated itinerant charge carriers:

$$\frac{1}{C} = \frac{d}{\epsilon_0 \epsilon_r A} - \frac{S}{\epsilon_0 \epsilon'_r A \sqrt{|n|}}, \quad (5)$$

where the dimensionless parameter S characterizes the strength of the correlation, which can be experimentally determined through fitting. The expressions and values for S for the different theoretical scenarios can be found in Table I. To fit Eq. (5) to our data, we express the carrier density as $|n| = \alpha |V_g - V_0|$, where V_g is the gate voltage, V_0 is the gate voltage where the itinerant charge-carrier density is zero, and α is the lever arm. We determine α from the Landau levels that emerge in magnetotransport (see Supplemental Material S1 [31]).

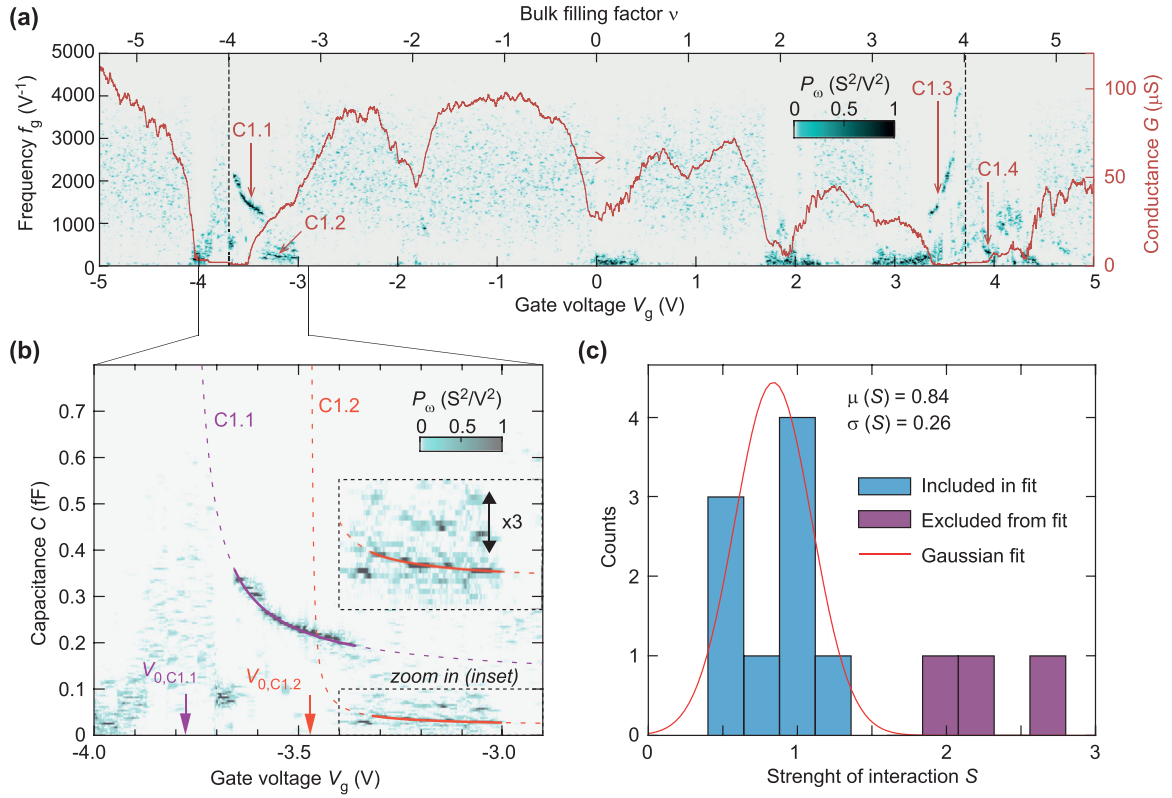


FIG. 6. Observation of negative compressibility and determining the interaction strength S . (a) Power spectrum P_ω vs capacitance C and gate voltage V_g on constriction C1. The conductance trace (right vertical axis) is included for easy comparison. (b) Zoom-in of P_ω near the band insulators at $\nu = -4$. Equation (5) is fit to two frequency components. The inset is scaled vertically by a factor 5 to highlight component C1.2. (c) Histogram of all the values of S determined from fitting and determining the mean of S .

B. Determining the strength of the interaction

Figure 6(b) shows the power spectrum of constriction C1 close to the band gap at $\nu = -4$. We identify and determine the maxima of two frequency components and fit Eq. (5) to extract S . The resulting excellent fit demonstrates that the $n^{-1/2}$ dependence in our model provides a good description of the gate-voltage-dependent frequency observed in the experiments. We perform this analysis on 12 frequency components from five different samples that are close to the magic angle: constrictions C1, C2, and C3 on device D1, and devices D2 and D3. The obtained values of S are summarized in Fig. 6(c), and the complete fitting results are presented in the Supplemental Material S3 [31]. The mean value of S is found to be

TABLE I. Expressions for the S in different correlated electron models compared to the experimental value. The abbreviation WC denotes the Wigner crystal scenario, while HF denotes the Hartree-Fock model in the exchange scenario.

	S	Value
WC	$\frac{3\eta_T}{32\pi}$	0.12
	$\frac{1}{1}$	
HF, unpolarized	$\frac{2\sqrt{2}\pi^{3/2}}{1.414}$	0.064
HF, polarized	$\frac{2\sqrt{2}\pi^{3/2}}{1.414}$	0.090
Experiment	–	0.84 ± 0.26

$\mu(S) = 0.84$ with a standard deviation of $\sigma(S) = 0.26$. Three outliers in Fig. 6(c) were excluded from calculating the mean value due to relatively large uncertainty bounds resulting from the fitting procedure.

C. Analysis with a fixed strength of the interaction

Next, we refine our model by fixing the parameter S to the mean value of $S = 0.84$, i.e., we account for all our data from devices close to the magic angle (the constrictions C1, C2, C3 and devices D2, D3) and band-gap transitions using one single, fixed value of S . This allows us to fit the subset of frequency components that occur within a narrow gate voltage range, expanding our dataset to include 18 frequency components. Note that in this refined model, both the vertical offset and steepness of the curve are solely determined by the size of the confinement A , while V_0 determines the horizontal position. The fitting results are presented in Fig. 7, where the vertical axis represents the inverse capacitance $1/C$, and the horizontal axis represents the average distance between the charge carriers $a = \alpha\sqrt{|V - V_0|}$. Each frequency component is labeled using the format “xx.y,” where “xx” is the constriction or device number, and “y” is the number of the frequency component. According to Eq. (5), the resulting maxima should fall along the straight line determined by the fit. Remarkably, using a fixed value of S provides excellent fits to all the data, regardless of the filling factor or the band where the frequency component is observed. The remaining

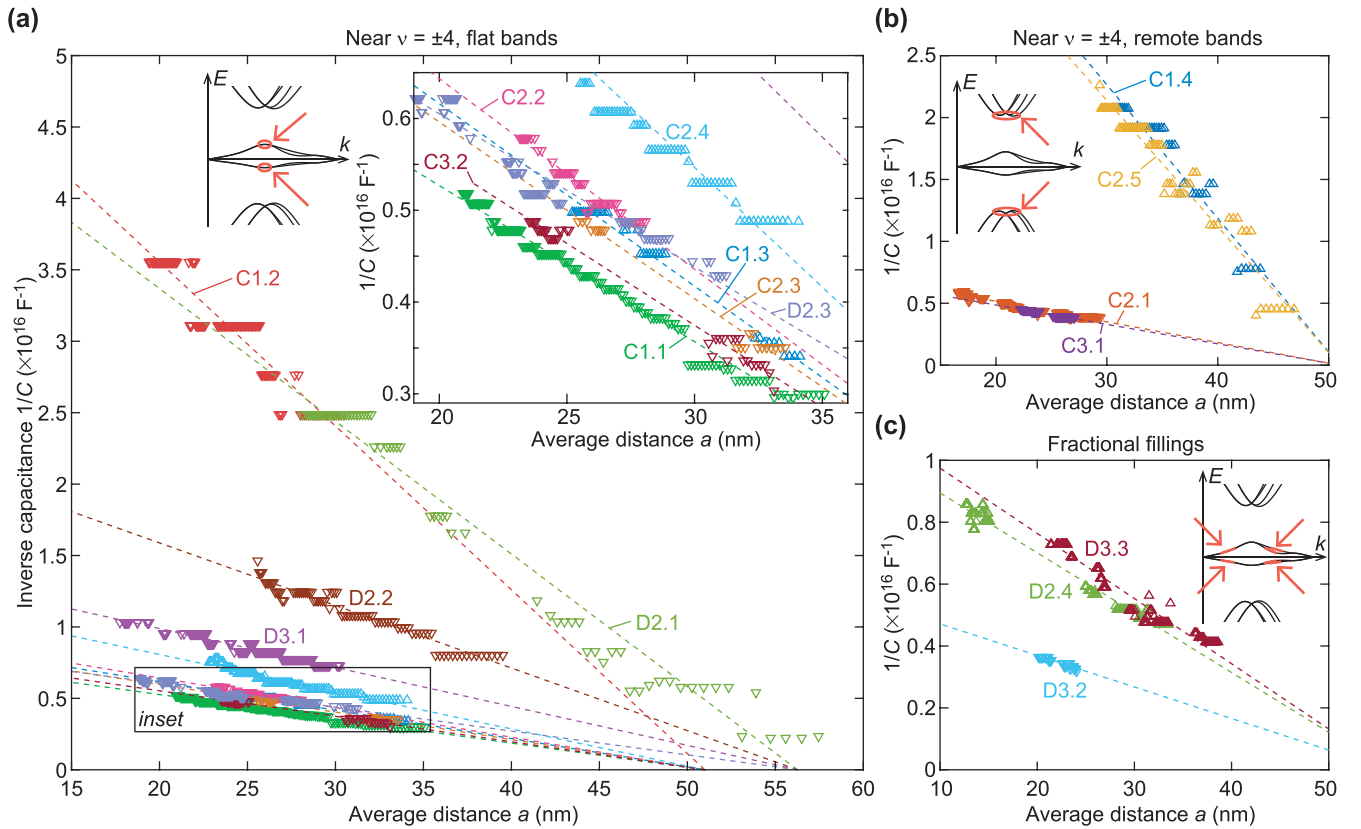


FIG. 7. Maxima in the power spectrum used to fit Eq. (5), plotted with $1/C$ on the vertical axes and the average distance between carriers $1/\sqrt{n} = a$ on the horizontal axes such that Eq. (5) becomes a straight line. The fits to each frequency component are made with a fixed value of $S = 0.84$. The frequency components are divided into panels such that (a) shows components found near $\nu = \pm 4$, on the side of the flat band (see the simplified band structure in the inset), (b) shows components found near $\nu = \pm 4$, on the side of the remote band, and (c) shows frequency components which are found near fractional fillings of the superlattice.

plots of the frequency components, including the fits and the fitted values of A and V_0 , are presented in the Supplemental Material S3 [31].

It is noteworthy that we also find periodic Coulomb oscillations that are well described by Eq. (5) close to the insulating states that form at fractional superlattice fillings [Fig. 7(c)]. These include components D2.4 found near $\nu = 2$, D3.2 near $\nu = -2$, and D3.3 near $\nu = 3$. The latter findings clearly demonstrate that a single-particle band gap is not necessary for confined regions to arise in the sample; instead, the charge gap arising from the correlated insulating states is sufficient. The fact that they are well described by Eq. (5), assuming a zero itinerant charge-carrier density at V_0 in the partially filled band, is also in line with the opening of a correlation-induced energy gap near the integer fillings of the superlattice.

D. Size and twist angle of the charge islands

Within this section we delve deeper into the results of our modeling and fitting analysis to evaluate their alignment with the scenario we proposed in Sec. III involving twist-angle domains. By comparing V_0 to the voltage where we pinpoint the center of the band gap in the bulk, we can estimate the deviation of the twist angle. We do this for constriction C1, and find that components C1.1, C1.2, C1.3, C1.4 deviate -0.023° , 0.016° , 0.011° , and -0.003° , respectively, from the

bulk value of 1.022° . These twist-angle variations are in line with observations in the literature [23]. This shows that minute twist-angle variations of only a few percent from the average bulk value suffice to produce the confinements observed in this work. Figure 8 displays the empirical cumulative distribution function (CDF) of the sizes (\sqrt{A}) of the 18 charge islands extracted from our fits on all frequency components. These sizes are consistent with the dimensions of our samples and similar to the experimental twist-angle maps obtained by Uri *et al.* [23]. A notable difference is that we find no substantially smaller ($\sqrt{A} < 125$ nm) or larger ($\sqrt{A} > 425$ nm) areas in our experiments. We note that small areas are usually embedded into a larger twist-angle domain that exhibits more uniformity, causing twist-angle boundaries that can couple to the charge island to be absent [23]. On the other hand, large domains are less likely to form a detectable charge island, since the large circumference makes it less probable that the entire surrounding region is insulating at the same time. Considering these factors, our size distribution aligns reasonably well with the literature, validating our model and the obtained value of $S \approx 0.84$.

V. NATURE OF THE CORRELATED STATE

Our work provides compelling evidence for a negative capacitance contribution within confined regions of tBLG.

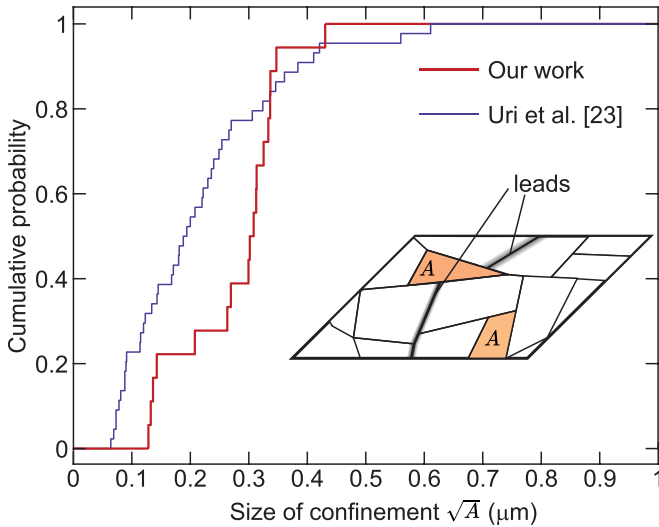


FIG. 8. Empirical cumulative distribution function (CDF) of the size of the confinements \sqrt{A} compared to the sizes of twist-angle domains estimated from the results of Uri *et al.* [23]. Insert shows a schematic of the confinements and the “leads” along the twist-angle boundaries where transport is thought to occur.

However, the nature of the correlated state remains uncertain. The analysis has established the $1/\sqrt{|n|}$ dependence of the inverse capacitance, consistent with both an exchange contribution or a Wigner crystal phase. However, the value of $S \approx 0.84$ is significantly larger than the expectation for both the Wigner and exchange scenarios (Table I). Nevertheless, several experimental observations may help clarify the nature of the correlated state:

(1) The observation of regular Coulomb oscillations suggests that the spin- or valley degree of freedom is not significant for the addition energy in the confined region.

(2) Substantial changes in the polarization of magnetic moments with magnetic field, including the disappearance of correlated insulating phases at high magnetic fields (see Supplemental Material S1 [31]), indicate that the Zeeman energy exceeds the exchange-induced energy gap. At a magnetic field of 9 T, the Zeeman energy in the order of 1 meV should dominate over other spin contributions, leading to a fully polarized electron gas. Consequently, if the electron gas is not polarized at zero field, the change in polarization between 0 and 9 T would lead to a frequency increase. For example, we would expect a frequency increase of 72% as $\xi \rightarrow 1$ for the 1100 V^{-1} component in Fig. 4(b). Instead, an indication of a change in the Coulomb oscillation frequency is observed in none of our measurements; additional examples are included in the Supplemental Material S9 [31].

(3) If the charge carriers are fully out-of-plane polarized at $B = 0$ T, no change in the Coulomb oscillation frequency is anticipated in the exchange scenario. However, no manifestation of such ferromagnetism such as an anomalous Hall effect [57] is observed, nor do we observe hysteresis when sweeping the magnetic field from -9 to 9 T and vice versa (see Supplemental Material S8 [31]).

(4) The carrier density dependence of the polarization of magnetic moments in the fluid phase is expected to be

strong [14], potentially leading to significant deviations from the observed $1/\sqrt{n}$ dependence of the inverse capacitance in the exchange scenario.

(5) Describing frequency components with the same value of S regardless of whether they are found near a correlated or band insulator is unexpected in the case of exchange contributions, according to theoretical simulations [58], because the spin/valley polarization varies for each energy gap that opens in tBLG [14].

(6) Theoretical models that take short-range interactions into account indicate that strong negative contributions to the capacitance are not anticipated close to the band insulating states at $\nu = \pm 4$ [58].

The absence of clear signatures expected in the exchange scenario and the consistent value of S across different bands suggests that a Wigner crystal phase may provide a better explanation for the observed negative compressibility. The exchange energy in a Wigner crystal follows a scaling law of the form $E_X \propto \exp(-\gamma\sqrt{r_s})$ [59,60], where γ is of the order 1. As a consequence, the interaction energy of a Wigner crystal does not rely on the polarization ξ , providing an explanation for the six observations listed above. The higher value of S than expected for a Wigner crystal may be related to the average distance a being in the same order to the moiré wavelength λ , causing a fraction of charge carriers to obtain even lower energy states within the nonuniform potential landscape provided by the moiré lattice. Importantly, as shown in Appendix B, this effect also leads to the same $1/C \propto 1/\sqrt{n}$ dependence, consistent with the experimental findings. Further investigations, considering additional factors and refinements to the model, may provide a more detailed understanding of the presently observed correlated state in tBLG.

VI. CONCLUSIONS

This study demonstrates a negative electronic compressibility in confined regions of tBLG. The observed dependence of the inverse capacitance on the charge-carrier density, characterized by $1/C \propto 1/\sqrt{n}$, aligns with the presence of strongly correlated itinerant charge carriers. The magnetic field dependence and the similarity of the correlation strength parameter S across different bands suggest a limited role of exchange contributions, pointing towards Wigner crystallization as a likely explanation for the observed negative compressibility. These findings highlight the role of naturally occurring electrostatic confinements in tBLG that enable precise investigation of the ground-state energy of correlated states in this material.

Our research reveals two distinct phenomena rooted in the moiré physics of tBLG. The first phenomenon involves electrostatic confinements arising from variations in the twist angle. This effect hinges solely on the presence of moiré-induced energy gaps, while the flatness of the band is not important. Therefore, this phenomenon is not exclusive to samples near the magic angle, as evidenced in tBLG samples far from this angle (Supplemental Material S4, S6 [31]). The second phenomenon is the manifestation of negative compressibility within these confinements. In this case, the band flattening in tBLG plays a crucial role, since r_s is required

to be large. This gains support from control experiments, particularly one conducted on a sample where the twisted bilayer has relaxed. In this case we observe the absence of moiré minigaps, while the charging spectrum of a confinement in this sample shows no negative compressibility (Supplemental Material S6 [31]). Furthermore, we extend our investigation to samples with twist angles significantly deviating from the magic angle ($\theta \sim 0.65^\circ$ in Supplemental Material S5 and $\theta > 1.29^\circ$ in Supplemental Material S7 [31]). While these samples do exhibit an increase in frequency as the Fermi level approaches an energy gap, their evolution with gate voltage deviates from the trend specified in Eq. (5). In these instances, the parameter r_s may not be sufficiently large to induce negative compressibility in the full gate voltage range where the confinement is formed, a factor that can be attributed to the reduced band flattening compared to the magic angle.

While it is commonly believed that correlated effects are not significant in the remote bands due to the absence of correlated insulating states [61], our observation of negative compressibility in these bands [Fig. 7(b)] challenges this notion. An analysis of the band structure, including a Hartree-Fock correction, suggests that the observed negative compressibility may be attributed to a significant correlation-induced flattening of the band when the filling factor exceeds $|\nu| = 4$ (see Appendix C).

The size of a typical charge island, as illustrated in Fig. 8, is notably larger than the moiré wavelength ($\lambda = 13.8$ nm for a 1.02° twist angle). This suggests that the periodicity of the moiré potential remains a crucial factor within the charge island, and the negative compressibility is not solely a consequence of electrostatic confinement. Our experimental evidence strongly supports this idea, revealing a significant suppression of the kinetic energies of carriers within the confinement compared to single-layer or Bernal-stacked bilayer graphene. In essence, we have demonstrated how moiré-induced confinement can offer quantitative insights into the interaction energies of correlated effects in tBLG by accurately measuring the local charging energy. This is the principal achievement of our work and has significant implications for understanding and manipulating correlated phases in moiré materials.

The source data and MATLAB code underlying this paper are available at Ref. [62] upon publication of this manuscript.

ACKNOWLEDGMENTS

The authors thank C. Volk and J. Sonntag for experimental support; F. Volmer, T. Ouaj, and M. Schmitz for assistance during sample fabrication; S. Trelenkamp and F. Lentz for electron-beam lithography, B. Shklovskii for correcting Eq. (2); and L. Gaudreau and M. Morgenstern for discussions. This work was supported by FLAG-ERA Grants No. 436607160 2D-NEMS, No. 437214324 TATTOOS, and No. 471733165 PhotoTBG by the Deutsche Forschungsgemeinschaft (DFG, German Research Foundation) and by the Deutsche Forschungsgemeinschaft (DFG, German Research Foundation) under Germany's Excellence Strategy – Cluster of Excellence Matter and Light for Quantum Computing (ML4Q) EXC 2004/1 – 390534769, by the Deutsche

Forschungsgemeinschaft (DFG, German Research Foundation) within the Priority Program SPP 2244 (535377524), and from the European Research Council (ERC) under the European Union's Horizon 2020 Research and Innovation Program (Grant Agreement No. 820254). A.F., L.K., and D.M.K. acknowledge funding by the Deutsche Forschungsgemeinschaft (DFG, German Research Foundation) under RTG 1995 and within the Priority Program SPP 2244 “2DMP.” F.L. acknowledges support by the Austrian Science Fund (FWF), Project I-3827-N36, and by the COST Association, COST Action No. CA18234. This work was supported by the Max Planck–New York City Center for Nonequilibrium Quantum Phenomena. Fabrication of the samples was supported by the Helmholtz Nano Facility [63]. K.W. and T.T. acknowledge support from JSPS KAKENHI (Grants No. 19H05790, No. 20H00354, and No. 21H05233).

R.J.D. and A.R. performed the experiments. A.R. fabricated the samples, L.W. built the laser cutting setup, and K.W. and T.T. grew the hBN crystals. R.J.D. performed the data analysis, and the results were interpreted with the input of A.R., A.F., L.K., L.W., D.M.K., F.L., B.B., and C.S., R.J.D. wrote the manuscript with the input of A.R., A.F., L.K., L.W., D.M.K., F.L., B.B., and C.S.

APPENDIX A: FERMI SURFACE AREA EXTRACTED FROM THE QUANTUM OSCILLATIONS

The electrostatically induced shifts in the position of the Coulomb resonances provide important clues about the transport characteristics between the metal leads and the confined regions. We plot the phase of the Coulomb oscillations (which is proportional to the Coulomb resonance position) obtained from the FFT analysis of the two prominent frequency components [Fig. 4(b)] in Fig. 9(a). This reveals a quantum oscillation that is periodic in $1/B$, and the quantum oscillation frequency can be extracted from an additional FFT analysis of the phase [inset of Fig. 9(a)]. By monitoring the phase of the oscillations at different gate voltages, we can extract the quantum oscillation frequency and plot these as red squares in Figs. 9(b) and 9(c). Since these quantum oscillations have the same microscopic origin as the Shubnikov–de Haas (SdH) oscillations observed in the sample's bulk magnetoresistance (see Supplemental Material S1 [31]), we also add the SdH frequency as a comparison [blue dots in Fig. 9(b)]. The quantum oscillation frequencies obtained from the Coulomb oscillations form a straight line that intersects the charge neutrality point at zero magnetic field in Fig. 9(c). In contrast, the SdH frequency intersects with fractional superlattice fillings at zero magnetic field due to the Dirac revival effect in tBLG, which reconstructs the Fermi surface area at fractional fillings [14]. We observe the same disparity in a second device, labeled D4, which is presented in the Supplemental Material S7 [31]. At higher gate voltages, we note that the lever arm of the gate decreases, which explains why the quantum oscillation frequency from the Coulomb oscillations exhibits a more gradual slope [red dashed lines in Figs. 9(b) and 9(c)] compared to the SdH frequency component emerging from the charge neutrality point [blue lines in Fig. 9(b)].

The Onsager relation establishes a direct proportionality between the frequency of quantum oscillations and the

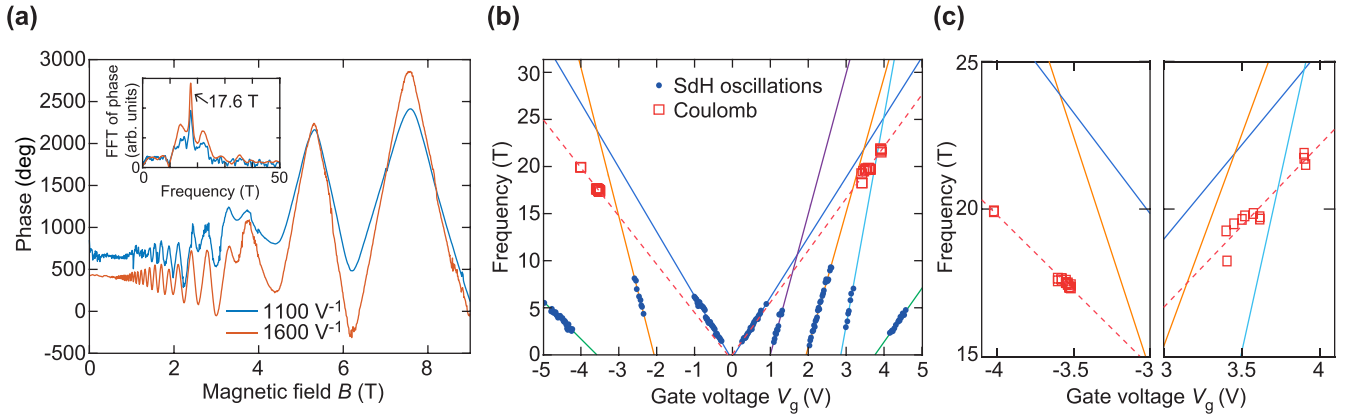


FIG. 9. (a) Phase of two prominent frequency components extracted from the fast Fourier transform in Fig. 4(b). (b) Quantum oscillation frequency of the magnetoresistance oscillations (see Supplemental Material S1 [31]), compared to the quantum oscillations in the phase of the Coulomb oscillations, as a function of gate voltage. (c) Zoom-in of the quantum oscillation frequency in the case of the Coulomb oscillation.

extremal Fermi surface area in momentum space [64]. In proximity to an energy gap, it logically follows that both the Fermi surface area should approach 0 nm⁻² and the frequency of quantum oscillations approaches 0 T. Therefore, the fact that the quantum oscillation frequency forms a linear relationship emanating from the charge neutrality point (CNP) is evidence for the absence of moiré-induced energy gaps for the charge carriers that are involved in the tunneling processes in and out of the charge islands.

APPENDIX B: GROUND-STATE ENERGY OF A WIGNER CRYSTAL IN A MOIRÉ SUPERLATTICE

In this Appendix we show that a periodic moiré potential may lead to a lowering of the ground-state energy of a Wigner crystal. Due to the periodic moiré potential, a fraction of charge carriers in the triangular Wigner lattice can obtain an even lower energy within the potential, lowering the ground-state energy even further than compared to a uniform background. If we assume a potential with minima ΔE , we can write this additional interaction energy contribution as

$$E_{\text{moiré}} = -An\Delta E\mathcal{R}, \quad (\text{B1})$$

where \mathcal{R} represents the effective fraction of charge carriers that are in the optimal position to profit from the moiré potential. For simplicity, we assume that $\mathcal{R} = a_{\text{moiré}}/a$ (where $a_{\text{moiré}}$ is the size of the moiré supercell) such that $\mathcal{R} = 1$ if $a_{\text{moiré}} = a$. Since $1/a = \sqrt{n}$, the moiré energy contribution becomes

$$E_{\text{moiré}} = -An^{3/2}\Delta Ea_{\text{moiré}}, \quad (\text{B2})$$

which leads to an additional capacitance contribution,

$$\frac{1}{C_{\text{moiré}}} = -\frac{3\Delta Ea_{\text{moiré}}}{4e^2A\sqrt{n}}, \quad (\text{B3})$$

with the same dependency on area and density as the interaction energy for a uniform background.

To estimate how much the ground-state energy is lowered, we compare to a tight-binding model of the moiré superstructure [65]. For small twist angles, the local rotation between unit cells in the top and bottom layers can be

neglected in favor of only considering a rigid displacement vector $\mathbf{d}(\mathbf{r})$ between the unrotated top and bottom layer. In the small angle approximation, $\mathbf{d}(\mathbf{r})$ can then be explicitly written as $\mathbf{d}(\mathbf{r}) \approx -\theta\hat{z} \times \mathbf{r}$. All displacements $\mathbf{d}(\mathbf{r})$ lie within the unit cell of the pristine lattice. Consequently, one can map each local configuration at a point \mathbf{r} of the moiré supercell to a rigid displacement $\mathbf{d}(\mathbf{r})$ in so-called configuration space mapped on the unit cell of the pristine lattice. Following the model we have outlined in [65], we map out tight-binding parametrizations in configuration space using a 10×10 grid in configuration space. We use a continuum elasticity model first suggested by Nam and Koshino [66] to calculate the effects of lattice reconstruction in tBLG. From our parametrization we extract the variations in on-site potential at a twist angle of ≈ 1 degrees, yielding $\Delta E \approx 14$ meV and $a_{\text{moiré}} = 14$ nm. From this analysis we find that the new correlation strength parameter $S = 0.16$, or an increase of 33% compared to the Wigner crystal with a uniform charge background. This result gives an idea of the order of magnitude of the correction but is likely an underestimation of the correction for two reasons. First, the interaction with the positive background is not included and will also result in an additional contribution due to the nonuniform charges of the underlying lattice. Second, we do not include effects of elasticity in the Wigner crystal; the Wigner lattice will likely deform to ensure a higher fraction is in the optimal position.

APPENDIX C: SUPPRESSION OF KINETIC ENERGY IN REMOTE BANDS

The atomic and electronic structure of tBLG is captured within an atomistic modeling approach [3,67,68] that relies on commensurate moiré unit cells with twist angle

$$\cos \theta = \frac{n^2 + 4nm + m^2}{2(n^2 + nm + m^2)}, \quad (\text{C1})$$

where $m, n \in \mathbb{N}$. For the simulations, we use $(n, m) = (32, 33)$, corresponding to a twist angle of $\theta = 1.018^\circ$ with $N = 12676$ carbon atoms per moiré unit cell. The positions of the carbon atoms are relaxed using classical force fields as outlined in Ref. [69]. The electronic structure is modeled

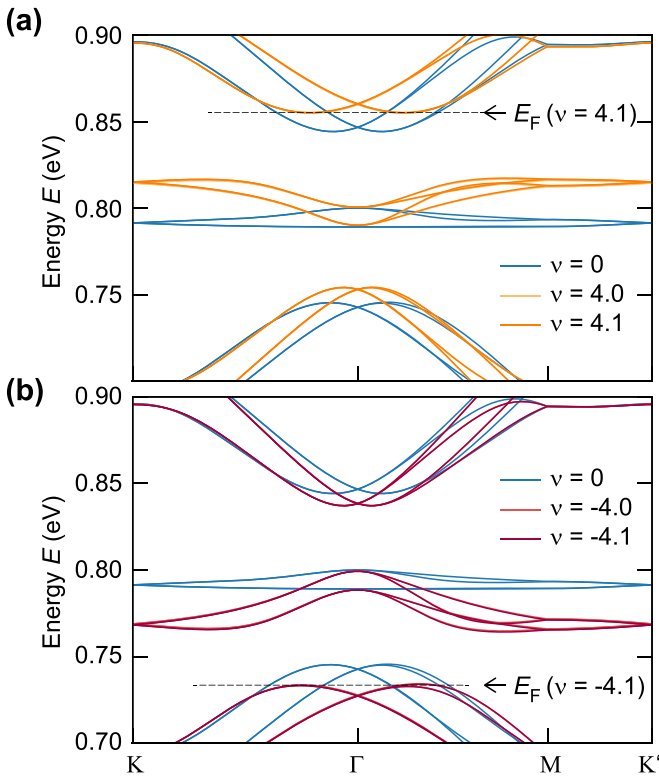


FIG. 10. Band structure of 1.018° tBLG in the presence of long-ranged electron-electron interactions. Hartree corrections render the band structure of tBLG filling dependent, which leads to a pinning of the van Hove singularity to the Fermi energy E_F and additional band flattening at the tip of the remote valence and conduction bands.

by a Slater-Koster tight-binding model of the carbon p_z orbitals using the parametrization adopted in Ref. [67]. Near the magic angle, long-ranged Coulomb interactions were shown to significantly renormalize the single-particle flat bands of tBLG [70–73] if the system is filled with electrons (holes), which can be captured within a self-consistent Hartree theory. Reference [71] demonstrated that within atomistic modeling approaches, the Hartree potential can effectively be parameterized by an on-site term of the form

$$V^H(\mathbf{r}) = V_0 \nu \sum_j \cos(\mathbf{G}_j \cdot \mathbf{r}), \quad (\text{C2})$$

where ν denotes the electronic filling $\nu = -4 \dots 4$ of the flat bands with respect to charge neutrality ($\nu = 0$), and \mathbf{G}_j are the three nonequivalent moiré reciprocal lattice vectors that differ by rotations around 120° . The value of the Hartree potential V_0 was found to be $V_0 = 5$ meV for the unscreened Coulomb interaction [71,74].

The (filling-dependent) band structure of 1.018° tBLG along the high-symmetry path $K - \Gamma - M - K'$ is shown in Fig. 10. At half-filling, the systems feature a set of flat bands that are well separated from the remote valence and conduction bands by a well-defined energy gap. Filling the flat bands of tBLG with electrons (upper panel) or holes (lower panel) shifts the energies at the K, K' points to higher (lower) energies due to the Hartree potential. Therefore the flattest sections of the bands follow the Fermi energy E_F ,

TABLE II. Thicknesses of the flakes used in each sample. Each thickness was determined by measuring the step height at the edge of the flake after fabrication in an atomic force microscope. The uncertainty on each thickness is 1 nm.

Sample	Bottom hBN (nm)	Top hBN (nm)	Graphite (nm)
D1	29	32	8
D2	32	24	5
D3	32	26	4
D4	35	37	10
D5	31	22	2
D6	22	22	3

which leads to a pinning of the van Hove singularities [73]. Furthermore, the Hartree potential affects the flatness of the tip of the valence (conduction) band manifold as indicated by the dashed line at filling factor $\nu = \pm 4.1$. This effect reduces the kinetic energy of charge carriers at the edge of the remote band, which may account for the prominent observation of a negative compressibility in this regime.

APPENDIX D: METHODS

1. Samples

Exfoliation: The flakes used for fabrication were mechanically exfoliated onto a silicon wafer with 90-nm-thick, thermally grown silicon dioxide [75]. Graphite flakes (“graphenium”) were obtained from NGS Naturgraphit GmbH.

Stacking: Device D1 was fabricated using the stack-and-tear method [5]. For device D1 we used polyvinyl alcohol (PVA) and polydimethylsiloxane (PDMS), and the stacking of the flakes was performed using the parameters described in Ref. [21]. For samples D2, D3, D5, and D6 we used a polybisphenol A carbonate (PC) stamp on top of a PDMS stamp [28]. In addition, the single-layer graphene flakes of these devices were pre-cut using a laser. Device D4 was produced using a PC stamp on PDMS [28]. For each sample, the thicknesses of the flakes are measured in tapping-mode atomic force microscopy (AFM), and the results are shown in Table II.

Laser cutting: Laser cutting was performed using a focused supercontinuum laser coupled into an optical microscope setup. The output of the laser was spectrally filtered to contain wavelengths of 400–550 nm, which maximizes the ratio of absorption in graphene compared to the absorption in Si for the used oxide thickness of 90 nm. The pulse duration on the sample is estimated to be few tens of picoseconds. The laser has a maximum repetition rate of 20 kHz but is typically operated at 4 kHz. The power can be varied using absorption filters, with a higher power increasing the width of the cut. Typical pulse energies used for laser cutting are 4 nJ, focused down to a submicrometer spot size, equivalent to a maximum intensity of approximately 2×10^{10} W/cm².

Fabrication: For fabrication we used a 50K/950K poly-methyl methacrylate (PMMA) double layer as our resist system (Allresist 631.09 and 679.04 both spin-coated at 4000 rpm and baked at 150° for 3 min per layer, with

a mixture of 3 parts isopropylalcohol and 1 part water as a developer) and e-beam lithography (Vistec EBPG5200+, 100 keV, clearance dose of $500 \mu\text{C}/\text{cm}^2$). The Hall-bar device was fabricated by first patterning holes into the top hBN layer. These holes were etched in a reactive ion etcher by first using a short oxygen plasma step (Oxford PL 100 / ICP at 20 W RF power, 40 sccm, as low pressure as possible $\sim 8 \mu\text{bar}$ for ~ 5 s) to remove contamination, followed by a CF_4 plasma etch (10 W, 40 sccm, low pressure), which significantly slows down at the graphene layer [29]. The duration of the CF_4 plasma step was adjusted to the top hBN thickness to prevent overetching into the bottom hBN layer. This was followed by another brief oxygen plasma step to remove the graphene, after which chrome and gold were deposited using e-beam evaporation, followed by a liftoff in warm acetone (without sonication). This results in a clean, one-dimensional edge contact to the tBLG [28]. Subsequently, the Cr/Au metal contacts and bond pads were patterned and evaporated using the same lift-off process.

For device D4 the fabrication was performed using a two-step process, where first the device geometry was structured using the CF_4 plasma and the electrodes were deposited in the second step. The contact resistances in this process are significantly higher than in the other devices, and this fabrication approach was not pursued further.

2. Twist-angle determination

Device D1: To determine the twist angle in the 750-nm constriction (C1), we extract the superlattice filling $n_s = 2.43 \times 10^{12} \pm 10^{12} \text{ cm}^{-2}$ from the Landau fan (Supplemental Material S1 [31]) and use the equation $n_s = 8\theta^2/\sqrt{3}a_l^2$ [8] (where $a_l = 0.246 \text{ nm}$ is the lattice constant of graphene) to find the twist angle in $\theta = 1.022^\circ$. For the remaining constrictions, we used the position of the band insulating features to determine the twist angle and find twist angles of 1.07° , 0.97° , and 0.91° for constrictions C2, C3, and C4, respectively.

Device D2: A $1 \mu\text{m}$ -wide Hall-bar geometry with a twist angle estimated from the Landau fan to be 0.97° comprise device D2. Additionally, we found an additional alignment between one of the graphene layers and the hBN, with a twist angle of $\sim 0.7^\circ$. We found no effects from this additional alignment on the charging spectra studied in this work. An optical image of this device, the conductance traces, and power spectra of this device are presented in the Supplemental Material S4 [31].

Device D3: A similar $1 \mu\text{m}$ -wide Hall-bar geometry without constrictions, device D3 broke down during the Landau fan measurement. Therefore we could only extract the lever arm of the back gate but not the position of the additional Landau fan. From the position of the insulating states, we are nevertheless able to estimate the twist angle to be 1.14° . An optical image of this device, the conductance traces, and power spectra of this device are also presented in the Supplemental Material S4 [31].

Device D4: Due to high contact resistances, it was not possible to extract the lever arm or the twist angle from magnetotransport experiments. Therefore, the twist angle was estimated using a parallel-plate capacitor model and the position of the insulating states. We estimate the twist angle to

vary between 1.29° and 1.45° on this sample. Sample imaging and measurement results are presented in the Supplemental Material S7 [31].

Device D5: On this device we did not obtain a clear additional Landau fan, but the lever arm could be estimated from the charge neutrality point. The twist angle was estimated from the position of high-resistance features found in transport measurements, which occur at $\nu = \pm 8$ in the low-twist-angle regime of this device [8]. We find a twist angle of 0.65° , and the results on this device are presented in Supplemental Material S5 [31].

Device D6: This device incorporated an additional WSe_2 (HQ graphene) into the stack which was picked up after picking up the tBLG. The tBLG graphene was relaxed back to near-Bernal stacking, since no evidence of moiré-induced satellite peaks was found. This device serves as a control sample, which is presented in the Supplemental Material S6 [31].

3. Experimental setup

Electrical characterization of all samples was performed in a $^3\text{He}/^4\text{He}$ wet dilution refrigerator (Oxford KelvinoxMX400) with a base temperature of 32.5 mK . All electrical wiring was directly connected to the sample with only a $1 \text{ k}\Omega$ pre-resistor in the BNC connector box used to connect to the instruments. The homebuilt amplifiers and IV converters were each placed in a shielded box outside the refrigerator. The total resistance between the BNC connector box to the sample holder was $1.24 \text{ k}\Omega$ for each line at room temperature. An out-of-plane magnetic field was applied with a superconducting magnet mounted in the liquid helium bath. We located the sample inside the coil of the magnet while avoiding magnetic materials in the insert to ensure a uniform magnetic field.

4. Data acquisition and analysis

Measurement of temperature-dependent resistance. The temperature-dependent resistance in Figs. 1(d) and 1(e) was measured using a homebuilt IV converter with a gain of 10×10^6 connected to two side contacts. This IV converter also applied a symmetric AC bias voltage to these contacts with an amplitude of $100 \mu\text{V}$ (rms) through a $1/10\,000$ voltage divider. The excitation signal was supplied by a Stanford SR830 lock-in amplifier operating at 69.6 Hz , and this apparatus also detected the signal from the IV converter. On the opposite side-contact pair, a differential amplifier with a gain of 1000 is connected to measure the voltage drop, and this signal is measured with a second lock-in amplifier. A voltage source (Yokogawa 7651) was connected to the gate through a $1\text{-M}\Omega$ resistor. The measurement was performed during the condensing of the mixture, circulating of the mixture and cooldown to base temperature of the dilution refrigerator. During this procedure, the gate voltage was constantly swept, and at each data point the temperature on the mixing chamber plate is recorded. During the cooldown procedure, the mixing chamber rapidly cools once the condensed mixture enters; therefore reliable measurements of the temperature between $\sim 2.5 \text{ K}$ and $\sim 4.5 \text{ K}$ were not possible. The resulting data is plotted on a meshed grid with interpolation using the MATLAB “pcolor” function.

Two-point conductance measurements. The conductance traces used to construct the power spectra are obtained by a two-point measurement of the conductance using the home-built IV converter and an AC bias of $100\ \mu\text{V}$ rms at a frequency of $69.6\ \text{Hz}$. The voltage source for the gate (Yokogawa 7651) was set to a range of $10\ \text{V}$, giving a resolution of $100\ \mu\text{V}$, and this is supplied to the system through a twisted-shielded cable with a low-pass filter with a cut-off frequency of $1.6\ \text{kHz}$ to reduce output noise. The resolution of $100\ \mu\text{V}$ is also the step size at which the gate voltage is swept, resulting in a Nyquist frequency of $5000\ \text{V}^{-1}$. For the bias spectroscopy data in Fig. 3, an additional voltage source was used to apply a symmetric DC bias.

Determination of the power spectra. To calculate the power spectra P_ω , we first perform a windowed autocorrelation on the gradient of the conductance with the MATLAB function “corrgram” [76]. We use a window of 200 samples, with an maximum lag of 200 points and overlap between the windows of 90%. Note that with this window we can only resolve frequency components $f_g > 50\ \text{V}^{-1}$. We then calculate the Fourier transform of the autocorrelation function using the MATLAB implementation “ezfft” [77]. By the convolution theorem, this approach is equivalent to calculating $|\mathcal{F}\{dG/dV_g\}|^2$.

Fitting to the power spectra. To fit Eq. (5) to our data, we find the maxima in the power spectra at each gate voltage. Due to the limited frequency resolution, this can lead to multiple

gate voltage values having the same capacitance in Fig. 7, but this is not a problem for the least-squares fitting procedure. We then load this into the curve-fitting tool “cftool” in MATLAB. We then manually select the correct maxima that belong to a single frequency component, and fit Eq. (5). cftool automatically calculates the 95% confidence interval, which defines the error in the fitting results presented in this work. We find the hBN thickness d from AFM scanning the stack before fabrication; their values are shown in Table II under the column: “bottom hBN.” The lever arm α is extracted during the extraction of the twist angle, as described above.

Magnetic field dependence. For Fig. 4(b) the fast Fourier transform was calculated at each magnetic field using the standard FFT implementation in MATLAB. This fast Fourier transform gives a complex number with which the angle can be calculated to obtain the phase. The resulting phase was unwrapped to obtain the continuous signal shown in Fig. 9(a). To find the frequency of the phase in $1/B$ as shown in the insert of Fig. 9(a), the phase signal was interpolated using a spline interpolation on a grid that is equally spaced in $1/B$. After this the FFT can be calculated to find the quantum oscillation frequency. The resulting frequencies are shown as red squares in Figs. 9(b) and 9(c). The same interpolation approach is taken on the magnetoresistance data (presented in Supplemental Material S1 [31]). After this, we find the maxima at each B field and manually select the correct frequency components, which are shown as blue dots in Fig. 9(b).

-
- [1] J. M. B. Lopes dos Santos, N. M. R. Peres, and A. H. Castro Neto, Graphene bilayer with a twist: Electronic structure, *Phys. Rev. Lett.* **99**, 256802 (2007).
- [2] E. Suárez Morell, J. D. Correa, P. Vargas, M. Pacheco, and Z. Barticevic, Flat bands in slightly twisted bilayer graphene: Tight-binding calculations, *Phys. Rev. B* **82**, 121407(R) (2010).
- [3] G. Trambly de Laissardière, D. Mayou, and L. Magaud, Localization of Dirac electrons in rotated graphene bilayers, *Nano Lett.* **10**, 804 (2010).
- [4] R. Bistritzer and A. H. MacDonald, Moiré bands in twisted double-layer graphene, *Proc. Natl. Acad. Sci. USA* **108**, 12233 (2011).
- [5] Y. Cao, J. Y. Luo, V. Fatemi, S. Fang, J. D. Sanchez-Yamagishi, K. Watanabe, T. Taniguchi, E. Kaxiras, and P. Jarillo-Herrero, Superlattice-induced insulating states and valley-protected orbits in twisted bilayer graphene, *Phys. Rev. Lett.* **117**, 116804 (2016).
- [6] A. Kerelsky, L. J. McGilly, D. M. Kennes, L. Xian, M. Yankowitz, S. Chen, K. Watanabe, T. Taniguchi, J. Hone, C. Dean, A. Rubio, and A. N. Pasupathy, Maximized electron interactions at the magic angle in twisted bilayer graphene, *Nature (London)* **572**, 95 (2019).
- [7] Y. Xie, B. Lian, B. Jäck, X. Liu, C.-L. Chiu, K. Watanabe, T. Taniguchi, B. A. Bernevig, and A. Yazdani, Spectroscopic signatures of many-body correlations in magic-angle twisted bilayer graphene, *Nature (London)* **572**, 101 (2019).
- [8] Y. Cao, V. Fatemi, A. Demir, S. Fang, S. L. Tomarken, J. Y. Luo, J. D. Sanchez-Yamagishi, K. Watanabe, T. Taniguchi, E. Kaxiras, R. C. Ashoori, and P. Jarillo-Herrero, Correlated insulator behaviour at half-filling in magic-angle graphene superlattices, *Nature (London)* **556**, 80 (2018).
- [9] Y. Choi, J. Kemmer, Y. Peng, A. Thomson, H. Arora, R. Polski, Y. Zhang, H. Ren, J. Alicea, G. Refael, F. von Oppen, K. Watanabe, T. Taniguchi, and S. Nadj-Perge, Electronic correlations in twisted bilayer graphene near the magic angle, *Nat. Phys.* **15**, 1174 (2019).
- [10] Y. Jiang, X. Lai, K. Watanabe, T. Taniguchi, K. Haule, J. Mao, and E. Y. Andrei, Charge order and broken rotational symmetry in magic-angle twisted bilayer graphene, *Nature (London)* **573**, 91 (2019).
- [11] J. Falson, I. Sodemann, B. Skinner, D. Tabrea, Y. Kozuka, A. Tsukazaki, M. Kawasaki, K. von Klitzing, and J. H. Smet, Competing correlated states around the zero-field Wigner crystallization transition of electrons in two dimensions, *Nat. Mater.* **21**, 311 (2022).
- [12] B. Tanatar and D. M. Ceperley, Ground state of the two-dimensional electron gas, *Phys. Rev. B* **39**, 5005 (1989).
- [13] Y. Cao, V. Fatemi, S. Fang, K. Watanabe, T. Taniguchi, E. Kaxiras, and P. Jarillo-Herrero, Unconventional superconductivity in magic-angle graphene superlattices, *Nature (London)* **556**, 43 (2018).
- [14] U. Zondiner, A. Rozen, D. Rodan-Legrain, Y. Cao, R. Queiroz, T. Taniguchi, K. Watanabe, Y. Oreg, F. von Oppen, A. Stern, E. Berg, P. Jarillo-Herrero, and S. Ilani, Cascade of phase transitions and Dirac revivals in magic-angle graphene, *Nature (London)* **582**, 203 (2020).
- [15] M. Yankowitz, S. Chen, H. Polshyn, Y. Zhang, K. Watanabe, T. Taniguchi, D. Graf, A. F. Young, and C. R. Dean, Tuning

- superconductivity in twisted bilayer graphene, *Science* **363**, 1059 (2019).
- [16] X. Lu, P. Stepanov, W. Yang, M. Xie, M. A. Aamir, I. Das, C. Urgell, K. Watanabe, T. Taniguchi, G. Zhang, A. Bachtold, A. H. MacDonald, and D. K. Efetov, Superconductors, orbital magnets and correlated states in magic-angle bilayer graphene, *Nature (London)* **574**, 653 (2019).
- [17] A. L. Sharpe, E. J. Fox, A. W. Barnard, J. Finney, K. Watanabe, T. Taniguchi, M. A. Kastner, and D. Goldhaber-Gordon, Emergent ferromagnetism near three-quarters filling in twisted bilayer graphene, *Science* **365**, 605 (2019).
- [18] M. Serlin, C. L. Tschirhart, H. Polshyn, Y. Zhang, J. Zhu, K. Watanabe, T. Taniguchi, L. Balents, and A. F. Young, Intrinsic quantized anomalous Hall effect in a Moiré heterostructure, *Science* **367**, 900 (2020).
- [19] N. Tilak, X. Lai, S. Wu, Z. Zhang, M. Xu, R. de Almeida Ribeiro, P. C. Canfield, and E. Y. Andrei, Flat band carrier confinement in magic-angle twisted bilayer graphene, *Nat. Commun.* **12**, 4180 (2021).
- [20] N. P. Kazmierczak, M. Van Winkle, C. Ophus, K. C. Bustillo, S. Carr, H. G. Brown, J. Ciston, T. Taniguchi, K. Watanabe, and D. K. Bediako, Strain fields in twisted bilayer graphene, *Nat. Mater.* **20**, 956 (2021).
- [21] A. Schäpers, J. Sonntag, L. Valerius, B. Pestka, J. Strasdas, K. Watanabe, T. Taniguchi, L. Wirtz, M. Morgenstern, B. Beschoten, R. J. Dolleman, and C. Stampfer, Raman imaging of twist angle variations in twisted bilayer graphene at intermediate angles, *2D Mater.* **9**, 045009 (2022).
- [22] C. N. Lau, M. W. Bockrath, K. F. Mak, and F. Zhang, Reproducibility in the fabrication and physics of Moiré materials, *Nature (London)* **602**, 41 (2022).
- [23] A. Uri, S. Grover, Y. Cao, J. A. Crosse, K. Bagani, D. Rodan-Legrain, Y. Myasoedov, K. Watanabe, T. Taniguchi, P. Moon, M. Koshino, P. Jarillo-Herrero, and E. Zeldov, Mapping the twist-angle disorder and Landau levels in magic-angle graphene, *Nature (London)* **581**, 47 (2020).
- [24] J. M. Park, Y. Cao, K. Watanabe, T. Taniguchi, and P. Jarillo-Herrero, Flavour Hund's coupling, Chern gaps and charge diffusivity in Moiré graphene, *Nature (London)* **592**, 43 (2021).
- [25] C. R. Dean, A. F. Young, I. Meric, C. Lee, L. Wang, S. Sorgenfrei, K. Watanabe, T. Taniguchi, P. Kim, K. L. Shepard, and J. Hone, Boron nitride substrates for high-quality graphene electronics, *Nat. Nanotechnol.* **5**, 722 (2010).
- [26] R. Ribeiro-Palau, S. Chen, Y. Zeng, K. Watanabe, T. Taniguchi, J. Hone, and C. R. Dean, High-quality electrostatically defined Hall bars in monolayer graphene, *Nano Lett.* **19**, 2583 (2019).
- [27] E. Icking, L. Banszerus, F. Wörtche, F. Volmer, P. Schmidt, C. Steiner, S. Engels, J. Hesselmann, M. Goldsche, K. Watanabe, T. Taniguchi, C. Volk, B. Beschoten, and C. Stampfer, Transport spectroscopy of ultraclean tunable band gaps in bilayer graphene, *Adv. Electron. Mater.* **8**, 2200510 (2022).
- [28] L. Wang, I. Meric, P. Y. Huang, Q. Gao, Y. Gao, H. Tran, T. Taniguchi, K. Watanabe, L. M. Campos, D. A. Muller, J. Guo, P. Kim, J. Hone, K. L. Shepard, and C. R. Dean, One-dimensional electrical contact to a two-dimensional material, *Science* **342**, 614 (2013).
- [29] T. Uwanno, T. Taniguchi, K. Watanabe, and K. Nagashio, Electrically inert h-BN/bilayer graphene interface in all-two-dimensional heterostructure field effect transistors, *ACS Appl. Mater. Interfaces* **10**, 28780 (2018).
- [30] M. Schmitz, S. Engels, L. Banszerus, K. Watanabe, T. Taniguchi, C. Stampfer, and B. Beschoten, High mobility dry-transferred CVD bilayer graphene, *Appl. Phys. Lett.* **110**, 263110 (2017).
- [31] See Supplemental Material at <http://link.aps.org/supplemental/10.1103/PhysRevB.109.155430> for additional bulk transport data on the 750-nm-wide constriction (S1), dependence of the Coulomb oscillations on the sample width (S2), the fitting results to determine the value of S (S3), the remaining power spectra and analysis with a fixed value of S (S4), additional results on a 0.65°-twisted sample D5 (S5), control experiments in the absence of moiré on sample D6 (S6), observation of Coulomb oscillations in sample D4 (S7), results on the Coulomb oscillations with magnetic field reversal on sample D4 (S8), and additional results on the negative electronic compressibility in a magnetic field (S9).
- [32] P. Stepanov, I. Das, X. Lu, A. Fahimniya, K. Watanabe, T. Taniguchi, F. H. L. Koppens, J. Lischner, L. Levitov, and D. K. Efetov, Untying the insulating and superconducting orders in magic-angle graphene, *Nature (London)* **583**, 375 (2020).
- [33] J. M. Park, Y. Cao, L.-Q. Xia, S. Sun, K. Watanabe, T. Taniguchi, and P. Jarillo-Herrero, Robust superconductivity in magic-angle multilayer graphene family, *Nat. Mater.* **21**, 877 (2022).
- [34] K. P. Nuckolls, M. Oh, D. Wong, B. Lian, K. Watanabe, T. Taniguchi, B. A. Bernevig, and A. Yazdani, Strongly correlated Chern insulators in magic-angle twisted bilayer graphene, *Nature (London)* **588**, 610 (2020).
- [35] S. L. Tomarken, Y. Cao, A. Demir, K. Watanabe, T. Taniguchi, P. Jarillo-Herrero, and R. C. Ashoori, Electronic compressibility of magic-angle graphene superlattices, *Phys. Rev. Lett.* **123**, 046601 (2019).
- [36] P. Stepanov, M. Xie, T. Taniguchi, K. Watanabe, X. Lu, A. H. MacDonald, B. A. Bernevig, and D. K. Efetov, Competing zero-field Chern insulators in superconducting twisted bilayer graphene, *Phys. Rev. Lett.* **127**, 197701 (2021).
- [37] Y. Saito, J. Ge, L. Rademaker, K. Watanabe, T. Taniguchi, D. A. Abanin, and A. F. Young, Hofstadter subband ferromagnetism and symmetry-broken Chern insulators in twisted bilayer graphene, *Nat. Phys.* **17**, 478 (2021).
- [38] S. Wu, Z. Zhang, K. Watanabe, T. Taniguchi, and E. Y. Andrei, Chern insulators, van Hove singularities and topological flat bands in magic-angle twisted bilayer graphene, *Nat. Mater.* **20**, 488 (2021).
- [39] C. Stampfer, E. Schurtenberger, F. Molitor, J. Güttinger, T. Ihn, and K. Ensslin, Tunable graphene single electron transistor, *Nano Lett.* **8**, 2378 (2008).
- [40] A. A. M. Staring, H. van Houten, C. W. J. Beenakker, and C. T. Foxon, Coulomb-blockade oscillations in disordered quantum wires, *Phys. Rev. B* **45**, 9222 (1992).
- [41] C. W. J. Beenakker, Theory of Coulomb-blockade oscillations in the conductance of a quantum dot, *Phys. Rev. B* **44**, 1646 (1991).
- [42] J. Güttinger, C. Stampfer, F. Libisch, T. Frey, J. Burgdörfer, T. Ihn, and K. Ensslin, Electron-hole crossover in graphene quantum dots, *Phys. Rev. Lett.* **103**, 046810 (2009).
- [43] M. Eich, F. Herman, R. Pisoni, H. Overweg, A. Kurzmann, Y. Lee, P. Rickhaus, K. Watanabe, T. Taniguchi, M. Sigrist, T. Ihn, and K. Ensslin, Spin and valley states in gate-defined bilayer graphene quantum dots, *Phys. Rev. X* **8**, 031023 (2018).

- [44] L. Banszerus, T. Fabian, S. Möller, E. Icking, H. Heiming, S. Trellenkamp, F. Lentz, D. Neumaier, M. Otto, K. Watanabe, T. Taniguchi, F. Libisch, C. Volk, and C. Stampfer, Electrostatic detection of Shubnikov–de Haas oscillations in bilayer graphene by Coulomb resonances in gate-defined quantum dots, *Phys. Status Solidi B* **257**, 2000333 (2020).
- [45] C. Gold, A. Kurzman, K. Watanabe, T. Taniguchi, K. Ensslin, and T. Ihn, Scanning gate microscopy of localized states in a gate-defined bilayer graphene channel, *Phys. Rev. Res.* **2**, 043380 (2020).
- [46] J. P. Eisenstein, L. N. Pfeiffer, and K. W. West, Negative compressibility of interacting two-dimensional electron and quasiparticle gases, *Phys. Rev. Lett.* **68**, 674 (1992).
- [47] K. Steffen, Compressibility and capacitance of quantum systems, Ph.D. thesis, Universität Augsburg, 2017.
- [48] G. Meissner, H. Namaizawa, and M. Voss, Stability and image-potential-induced screening of electron vibrational excitations in a three-layer structure, *Phys. Rev. B* **13**, 1370 (1976).
- [49] L. Bonsall and A. A. Maradudin, Some static and dynamical properties of a two-dimensional Wigner crystal, *Phys. Rev. B* **15**, 1959 (1977).
- [50] M. S. Bello, E. I. Levin, B. I. Shklovskii, and A. L. Efros, Density of localized states in the surface impurity band of a metal-insulator-semiconductor structure, *Sov. Phys. JETP* **53**, 822 (1981).
- [51] I. M. Ruzin, S. Marianer, and B. I. Shklovskii, Pinning of a two-dimensional Wigner crystal by charged impurities, *Phys. Rev. B* **46**, 3999 (1992).
- [52] H. Fu, B. I. Shklovskii, and B. Skinner, Correlation effects in the capacitance of a gated carbon nanotube, *Phys. Rev. B* **91**, 155118 (2015).
- [53] S. Joy and B. Skinner, Wigner crystallization at large fine structure constant, *Phys. Rev. B* **106**, L041402 (2022).
- [54] B. Skinner and B. I. Shklovskii, Anomalously large capacitance of a plane capacitor with a two-dimensional electron gas, *Phys. Rev. B* **82**, 155111 (2010).
- [55] L. Wang, Y. Wang, X. Chen, W. Zhu, C. Zhu, Z. Wu, Y. Han, M. Zhang, W. Li, Y. He *et al.*, Negative quantum capacitance induced by midgap states in single-layer graphene, *Sci. Rep.* **3**, 2041 (2013).
- [56] S. Ilani, L. A. K. Donev, M. Kindermann, and P. L. McEuen, Measurement of the quantum capacitance of interacting electrons in carbon nanotubes, *Nat. Phys.* **2**, 687 (2006).
- [57] N. Nagaosa, J. Sinova, S. Onoda, A. H. MacDonald, and N. P. Ong, Anomalous Hall effect, *Rev. Mod. Phys.* **82**, 1539 (2010).
- [58] G. Rai, L. Crippa, D. Călugăru, H. Hu, L. d. Medici, A. Georges, B. A. Bernevig, R. Valentí, G. Sangiovanni, and T. Wehling, Dynamical correlations and order in magic-angle twisted bilayer graphene, [arXiv:2309.08529](https://arxiv.org/abs/2309.08529).
- [59] B. Spivak and S. A. Kivelson, Phases intermediate between a two-dimensional electron liquid and Wigner crystal, *Phys. Rev. B* **70**, 155114 (2004).
- [60] M. Roger, Multiple exchange in ^3He and in the Wigner solid, *Phys. Rev. B* **30**, 6432 (1984).
- [61] I. Das, X. Lu, J. Herzog-Arbeitman, Z.-D. Song, K. Watanabe, T. Taniguchi, B. A. Bernevig, and D. K. Efetov, Symmetry-broken Chern insulators and Rashba-like Landau-level crossings in magic-angle bilayer graphene, *Nat. Phys.* **17**, 710 (2021).
- [62] Dataset: Negative electronic compressibility in charge islands in twisted bilayer graphene, Zenodo [10.5281/zenodo.7409456](https://zenodo.org/doi/10.5281/zenodo.7409456) (2024).
- [63] W. Albrecht, J. Moers, and B. Hermanns, HNF - Helmholtz Nano Facility, *JLSRF* **3**, A112 (2017).
- [64] L. Onsager, Interpretation of the de Haas–van Alphen effect, *London, Edinburgh, Dublin Philosophical Magazine J. Sci.* **43**, 1006 (1952).
- [65] T. Fabian, M. Kausel, L. Linhart, J. Burgdörfer, and F. Libisch, Half-integer Wannier diagram and Brown-Zak fermions of graphene on hexagonal boron nitride, *Phys. Rev. B* **106**, 165412 (2022).
- [66] N. N. T. Nam and M. Koshino, Lattice relaxation and energy band modulation in twisted bilayer graphene, *Phys. Rev. B* **96**, 075311 (2017).
- [67] M. Koshino, N. F. Q. Yuan, T. Koretsune, M. Ochi, K. Kuroki, and L. Fu, Maximally localized Wannier orbitals and the extended Hubbard model for twisted bilayer graphene, *Phys. Rev. X* **8**, 031087 (2018).
- [68] A. Fischer, L. Klebl, C. Honerkamp, and D. M. Kennes, Spin-fluctuation-induced pairing in twisted bilayer graphene, *Phys. Rev. B* **103**, L041103 (2021).
- [69] L. Klebl, Z. A. H. Goodwin, A. A. Mostofi, D. M. Kennes, and J. Lischner, Importance of long-ranged electron-electron interactions for the magnetic phase diagram of twisted bilayer graphene, *Phys. Rev. B* **103**, 195127 (2021).
- [70] F. Guinea and N. R. Walet, Electrostatic effects, band distortions, and superconductivity in twisted graphene bilayers, *Proc. Natl. Acad. Sci. USA* **115**, 13174 (2018).
- [71] Z. A. H. Goodwin, V. Vitale, X. Liang, A. A. Mostofi, and J. Lischner, Hartree theory calculations of quasiparticle properties in twisted bilayer graphene, *Electron. Struct.* **2**, 034001 (2020).
- [72] L. Rademaker, D. A. Abanin, and P. Mellado, Charge smoothening and band flattening due to Hartree corrections in twisted bilayer graphene, *Phys. Rev. B* **100**, 205114 (2019).
- [73] T. Cea, N. R. Walet, and F. Guinea, Electronic band structure and pinning of Fermi energy to Van Hove singularities in twisted bilayer graphene: A self-consistent approach, *Phys. Rev. B* **100**, 205113 (2019).
- [74] Z. A. H. Goodwin, V. Vitale, F. Corsetti, D. K. Efetov, A. A. Mostofi, and J. Lischner, Critical role of device geometry for the phase diagram of twisted bilayer graphene, *Phys. Rev. B* **101**, 165110 (2020).
- [75] K. S. Novoselov, D. Jiang, F. Schedin, T. J. Booth, V. V. Khotkevich, S. V. Morozov, and A. K. Geim, Two-dimensional atomic crystals, *Proc. Natl. Acad. Sci. USA* **102**, 10451 (2005).
- [76] N. Marwan, Windowed Cross Correlation (corrgram), <https://www.mathworks.com/matlabcentral/fileexchange/15299-windowed-cross-correlation-corrgram> (Accessed: 11 Jan 2022).
- [77] F. Moisy, EZFFT: An easy to use power spectrum (FFT), <https://www.mathworks.com/matlabcentral/fileexchange/22163-ezfft-an-easy-to-use-power-spectrum-fft> (Accessed: 18 Dec 2019).